JOURNAL OF AIRCRAFT
Vol. 33, No. 2, March–April 1996

Simulation and Analysis of V-22 Tiltrotor Aircraft Forward-Flight Flowfield

Tsze C. Tai*
U.S. Naval Surface Warfare Center, Bethesda, Maryland 20084

The flowfield about a wing–fuselage–nacelle configuration of the V-22 tiltrotor aircraft at a freestream Mach number of 0.345 and angles of attack ranging from 7 to 16 deg is simulated by using a multizone, thin-layer Navier–Stokes method. The flow conditions yield a Reynolds number of 18.2 × 10^6 based on the wing chord for flight at an altitude of 10,000 ft. Major flow features including the three-dimensional flow separation from viscous–vortex interactions observed experimentally are captured by the simulation. The massive separation from the wing and the fore fuselage–sponson region for flows at high angles of attack creates free vortices that pass by the rear fuselage region, including the tail section of the aircraft.

Introduction

THE tiltrotor aircraft combines the high-speed efficiency of a turboprop aircraft with the vertical takeoff and landing capabilities of a helicopter. Although the concept has been investigated for many years, it has only recently been developed into an operational prototype for military use.[1–5] The ability to take off and land anywhere and to fly like an aircraft has great potential for civil transport.[6] The ongoing military program will provide an important database for the civil application.

The development of the military version, the V-22 Osprey, is in the midst of aerodynamic refinements, among other developments. Because of its dual capabilities, the aircraft experienced design restrictions that adversely affect aerodynamic performance. For example, the wing has to be thick enough to house the heavy rotor shaft for power transmission and torsionally stiff enough to provide propulsor stability in airplane mode. As a result, the aircraft in its forward-flight mode has a drag coefficient higher than that of its fixed wing counterpart, and experiences a steep drag rise at high angles of attack. Furthermore, flying at poststall angles of attack can also cause tail buffeting as revealed in recent flight tests. The complexity of the flow makes accurate analytical predictions of aerodynamic performance and stability characteristics of the configuration very difficult. Evaluation of these designs would have to rely on experimental means that are inconvenient, time consuming, and in some cases, unable to provide insight into physical flow.

The prospects for developing useful analytical tools for such complex flows are brightened by recent advances made in the area of computational fluid dynamics (CFD). Raghavan et al.[7] applied a two-dimensional, implicit finite difference type thin-layer Navier–Stokes scheme to consider the flow past an isolated V-22 wing section under the downwash from a tiltrotor. The flow is equivalent to that of an airfoil traveling at an angle of attack of −90 deg. The vertical drag values found were rather inconclusive, which may be attributed to the difficulty in predicting the base pressures for most of the bluff bodies, in particular for the flat plate and XV-15 airfoil.

Later, Fejtek and Roberts[8] considered the flow over a rotor–wing configuration by using a three-dimensional, finite difference type thin-layer Navier–Stokes solver. The rotor was modeled as an actuator disc coupled to the flowfield with the aid of the solution blanking as used in the chimera overset grid approach. Results were obtained for both a rotor alone and a wing–rotor combination. Many of the complex flow features were captured including the fountain effect, and the leading- and trailing-edge separations. Although the wing surface pressures were generally 20% higher than the measured values, the scheme offers a significant improvement to the previous attempt by Raghavan et al.[7]

A more realistic V-22 geometry, a wing–fuselage–nacelle configuration, has been considered by Tai and Vorwald.[9] Similar to the Fejtek and Roberts' approach, the rotor power output was represented by specified disc loading imposed at the rotor boundary. However, in contrast to the previous work, a finite volume type Navier–Stokes flow solver was employed; and to accommodate the physical flow, a special grid topology having the grid centerline that coincides with the centerline of the rotor–nacelle assembly has been developed. Calculated outflow flowfields captured significant flow characteristics and the computed mean velocities at 25 ft hover height are in good agreement with flight test data as reported in Ref. 9.

All of these CFD-based aerodynamic analyses have focused on the hover flowfield. Limited application has been given to the forward-flight configuration. An attempt to simulate the V-22 aircraft flowfield in hover-to-transition flight mode was explored by Meakin.[10] Attention is directed toward the forward-flight mode in the present work. The objectives are to identify the source of drag rise and the angle-of-attack limit within the ability of the steady-state flow solution, and to provide timing-critical analysis to aerodynamic problems relevant to the subject aircraft. To achieve these objectives, the aircraft can be modeled by considering the wing–fuselage–nacelle configuration only without the complexity of the tail sections. The aircraft is assumed to be symmetric with respect to its centerline so that only half of the configuration needs to be modeled. Extension to the whole aircraft flowfield for evaluating the sideslip effect is planned.

Simulation Method

The simulation method, or the computational method employed includes two main elements: 1) the grid generation and 2) the flow solving. The description of the method therefore will be centered around these two topics, which are of equal importance.

Grid Generation and Grid Topology

A structured, curvilinear, body-conforming grid is employed. The surface grid is constructed from the manufacturer's blueprint with refinement based on data provided by

Presented as Paper 95-0045 at the AIAA 33rd Aerospace Sciences Meeting and Exhibit, Reno, NV, Jan. 9–12, 1995; received April 16, 1995; revision received Oct. 2, 1995; accepted for publication Oct. 8, 1995.

*Senior Research Scientist, Sea Based Aviation Office, Carderock Division. Associate Fellow AIAA.

Boeing Defense and Space Group (see Fig. 1). A cylindrical grid topology, which is basically made up of an H–O mixed type with H-type in the longitudinal plane and O-type in the crossflow plane, is adopted. The outer cylindrical surface is set at 7.7 chord lengths from the aircraft centerline. Assuming symmetry about the centerplane, only the right half of the aircraft needs to be modeled. The advantage of this grid topology is that it permits simple and accurate discretizing approximations and can be easily clustered in the viscous region. It is relatively fast for flow solving with good accuracy. Its primary disadvantage, however, is that it is difficult and time consuming for complex geometries.

The work is divided into three phases of increasing geometric complexity: 1) the wing-alone geometry, 2) the wing-fuselage combination, and 3) the final wing–fuselage–nacelle configuration. In this article, however, we will focus on the wing-alone and wing–fuselage–nacelle configuration cases only.

For the wing-alone case, the geometry is simple and the grid generation is rather straightforward. We first divide the whole domain into upper and lower regions. The multiblock scheme is applied to generate the common interface mesh that is then used as the base boundary in generating the basic grids separately for both regions. Three blocks were used for each of the regions. The two meshes are subsequently combined together into a single basic grid. The radial distances are then clustered near the surface and stretched in the outer region for shear layer development. The final grid for the wing-alone geometry has a total of 127 × 37 × 51 points in the longitudinal, circumferential, and radial directions, respectively.

In the case of the wing–fuselage–nacelle configuration, the geometry becomes extremely complex because of the nacelle mounted at the wingtip and the sponson protrusion at the bottom of the fuselage. To overcome this difficulty, a new successive multiblock grid generation procedure was developed. A brief description is given next for completeness.

The idea of the new procedure is to apply the usual elliptic grid generator in a multiblock domain successively, at least three or four times, to achieve the final desired grid. Basically, the procedure calls for two steps in grid generation. The first step performs the basic grid generation, and the second step is devoted to grid refinement. For the wing–fuselage–nacelle configuration, the whole domain is also divided into upper and lower regions, similar to the wing-alone case. The first step consists of the creation of the common interface mesh between the upper and lower regions, and the subsequent generation of the basic grids for both regions. Ten blocks are used for the upper region and 15 blocks for the lower one. The two meshes are then combined together into one single basic grid.

The highly skewed geometry between the fuselage and nacelle, as shown in Fig. 2, requires further grid refinements, i.e., the second step. In this step, we focus on the part of the basic grid that contains intersecting grid lines. These lines cut across each other causing negative cell volumes that are not acceptable to the flow solver. The local volume grid having intersecting grid lines is then taken out for regeneration. In so doing, we eventually open up a six-sided hole in the basic grid and use the six faces of the hole as new boundaries for the elliptic generator. Figure 3 shows the four faces taken from a hole near the nacelle–wing juncture in the basic grid. The resolution of the new boundaries is doubled to improve the quality of the resulting regional grid. Upon completion, there are still a few lines intersecting each other near the bluff juncture between the nacelle and the lower wing. Therefore, we need to open up a smaller hole within the new regional grid and apply the elliptic generator once more. The final grid, after viscous clustering, has a total of 156 × 105 × 51 points.

The NASA Ames 3DGRAPE code[11] is used for basic grid generation and CNS/ZONER code[12] for zoning and clustering. The latter has been modified to cluster the viscous region with a variety of spline curves composed of different spacing and numbers for the radial direction to be fitted.

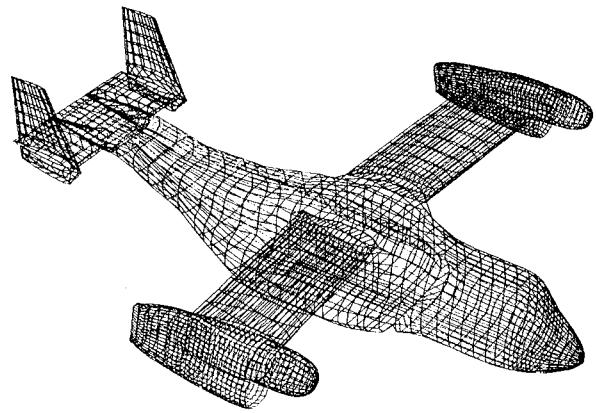

Fig. 1 Surface grid for V-22 tiltrotor aircraft.

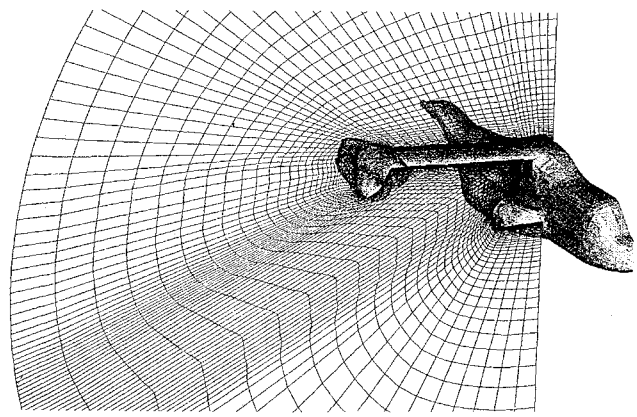

Fig. 2 Cross section of the overall basic grid.

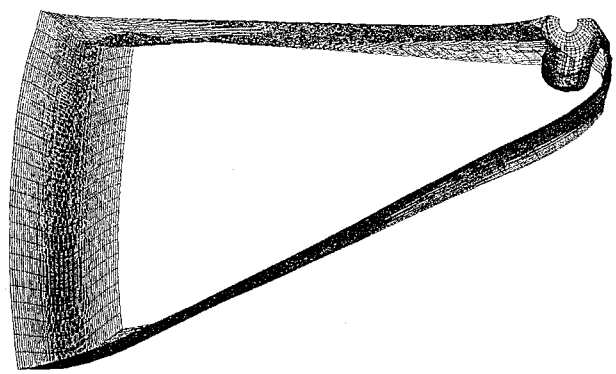

Fig. 3 Surfaces from a hole opened in the basic grid as boundaries for regional grid generation.

Flow Solver and Turbulence Model

The NASA Langley thin-layer Navier–Stokes code, namely the CFL3D code[13] with multizone capability, is used as the basic flow solver. Appropriate modifications to the code for applying specific boundary conditions are implemented. The code is based on a finite volume algorithm with a spatially factored diagonalized, implicit scheme. The upwind-biased-differencing technique is used for the inviscid terms and central differencing for all viscous terms. The method is globally second-order accurate and well suited for patched grids in a multizone domain.

The code is upgraded with a variety of turbulence models, including the basic Baldwin–Lomax algebraic model[14] and the Spalart–Allmaras one-equation model,[15] among others. These

turbulence models have been carefully examined and evaluated by Rumsey and Vatsa.[16] In the present work, the B–L algebraic model with a Degani–Schiff type modification[17] is used for cases with small-to-moderate angles of attack. For flow at high angles of attack, the B–L model starts to cause a convergence problem because of the unsteadiness from large flow separation, and so the Spalart–Allmaras turbulence model[15] is employed.

Multizone Technique and Boundary Conditions

The single basic grid, generated previously, is eventually divided into multizones for flow solving using the multizone technique.[18] In literature, the terms multizone and multiblock are generally interchangeable because a particular block of the grid generated is used also as a zone in the flow solving. In this article, however, we will distinguish the multizone from multiblock because they are not the same. In the case of the wing–fuselage–nacelle configuration, we have divided the single basic grid into 17 zones for flow solving, whereas the grid was generated with 25 blocks.

The division of the overall mesh into multizones depends primarily on the convenience in applying the boundary conditions. Having the same number of radial mesh points for both viscous and inviscid zones, such a division offers exact coincident boundaries between the zones. The main advantage of the approach is that the conservation of the spatial flux of mass, momentum, and energy between the zones is automatically satisfied. A total of 40 interface boundaries are set among the 17 zones in flow solving.

The boundary conditions for the Navier–Stokes flow solver are, within a particular zone: 1) freestream condition imposed at upstream (for the most forward zones only), 2) freestream pressure recovery in downstream (for the most rearward zones only), 3) characteristic form of inflow–outflow at the cylindrical outer boundary, and 4) viscous nonslip flow at all solid surfaces (wing, fuselage, and nacelle). The inlet and outlet of the nacelle are closed for simplicity and the disc loading at the rotor is neglected. The reason for neglecting the disc loading is that there are only 5–6-ft/s velocity differentials at the rotor disc, which may have little effect on the resulting flowfield.

Results and Discussion

Simulated results of the flow over the wing-alone geometry and the wing–fuselage–nacelle configuration subject to a typical forward-flight Mach number at a range of angles of attack are obtained and discussed. For the wing-alone case, the flow conditions were set according to the available wind-tunnel test data. For the case of the wing–fuselage–nacelle configuration, the flow conditions were chosen to coincide with the ongoing flight test program by the U.S. Navy.

All computations were performed on the Numerical Aerodynamic Simulation (NAS) supercomputer facility at NASA Ames Research Center. Converged steady-state results were obtained in about 4000–5000 iterations requiring approximately 7–8 h of Cray C-90 CPU time.

Wing-Alone Case

The wing-alone case is considered simply to validate the present CFD results with available experimental data. The wing platform is the same as the one used in the wind-tunnel tests performed by Jenks and Narramore.[19] The airfoil profile is exactly that used in the V-22 aircraft, which has a thickness ratio of 23%. The airfoil was designed after the era of supercritical wing research in the late 1960s and early 1970s, and so is the new airfoil technology for general aviation. The experimental model was a 23% JVX wing tested in the two-dimensional insert of Boeing Supersonic Wind Tunnel with end plates on the wing.

The flow conditions used for the wing-alone case were at a freestream Mach number of 0.13 and at an angle of attack of 7 deg with a Reynolds number of 2.0×10^6, coinciding with the wind-tunnel test condition. The particle trace of the simulated flow is shown in Fig. 4. The flow is all attached with boundary layers developing along the chordwise direction. Since there is no forward sweep of the wing, there is virtually no crossflow occurring in the computed results for this low angle-of-attack condition. Also, because of the end plate, there are no tip vortices generated. If the airfoil were of the old NACA-type design, the flow might have separated, considering the high thickness ratio involved.

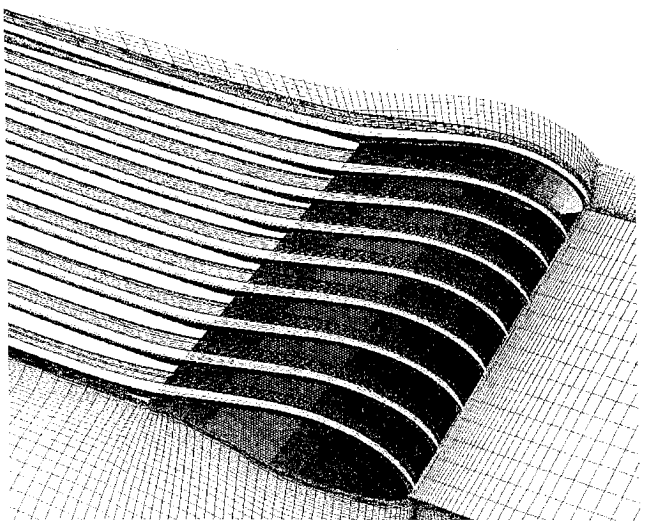

Fig. 4 Particle trace over the wing-alone geometry at $M_\infty = 0.13$, $\alpha = 7$ deg, and $Re_\infty = 2 \times 10^6$.

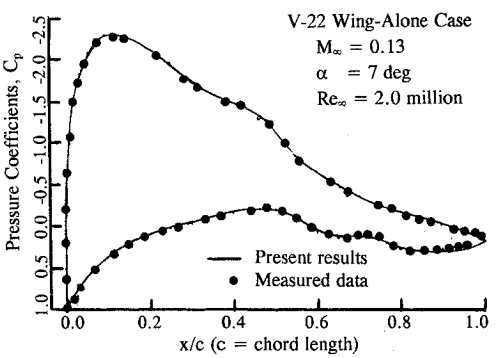

Fig. 5 Comparison of computed pressures over the wing-alone geometry with measured data.

Comparison of the computed chordwise pressures distribution with the experimental measurements is given in Fig. 5. Very good agreement between the calculated results and the measurements is observed. Discontinuities in the computed pressure contours forward of the leading edge are the result of a zonal boundary. Note that the present results yield much closer agreement between the theory and experiment than that predicted by a two-dimensional, potential-flow code of Bauer, Garabedian, and Korn (BGK) used in Ref. 19. The BGK code was well accepted by the aerospace community about 15–20 years ago; the supercomputer and its byproduct, the discretized Navier–Stokes solution, were not then available.

Wing–Fuselage–Nacelle Configuration

For the wing–fuselage–nacelle configuration, simulated results are obtained for a freestream velocity of 220 kn at angles of attack of 7, 12, and 16 deg at an altitude of 10,000 ft. These conditions yield a Mach number of 0.345 and a Reynolds number of 18.2×10^6, based on the wing chord length of 10 ft (as opposed to the 8.33-ft chord used in the prototype aircraft). All computations were performed by assuming the flow was fully turbulent, and so there is no need to specify the transition

location. The results are presented in the form of particle trace, velocity vector plots, and pressure distributions over the configuration. The case of angle of attack of 16 deg will be discussed more extensively because of important physical features involving separated flow and its related effects on the maneuvering aerodynamics of the aircraft.

Particle Trace

The particle traces of the streamlines emanating from various stations at the fuselage, wing, and nacelle are shown in Figs. 6, 7, and 8 for flow at angles of attack of 7, 12, and 16 deg, respectively. The flow over the wing is attached for the case of angle of attack at 7 deg. However, instantaneous particle traces originating at the sponson rolled up in the rear region, creating free vortices downstream while converging into the mainstream.

As the angle of attack increases to 12 deg, the flow on the fuselage and most of the wing remains mostly attached. However, streamlines over the top of the fuselage start to separate and roll up downstream, merging with those from the sponson. These separations are mainly because of convergence of viscous streamlines inside the boundary layer. The phenomenon is known as viscous–inviscid interaction.

Further increase in the angle of attack to 16 deg causes massive separation to take place over the upper wing surface, near the wing–nacelle juncture and from the midwing to the wing root, as shown in Fig. 8. Unlike most aircraft aerodynamic flows, the crossflow over the wing flows inboard towards the fuselage. The reason for this unusual crossflow direction seems to be because of the 6-deg forward swept angle of the V-22 wing.

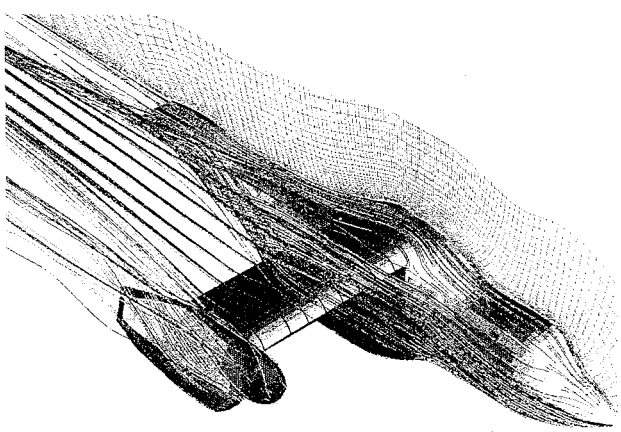

Fig. 6 Particle trace over the wing–fuselage–nacelle configuration at $M_\infty = 0.345$, $\alpha = 7$ deg, and $Re_\infty = 18.2 \times 10^6$; perspective view.

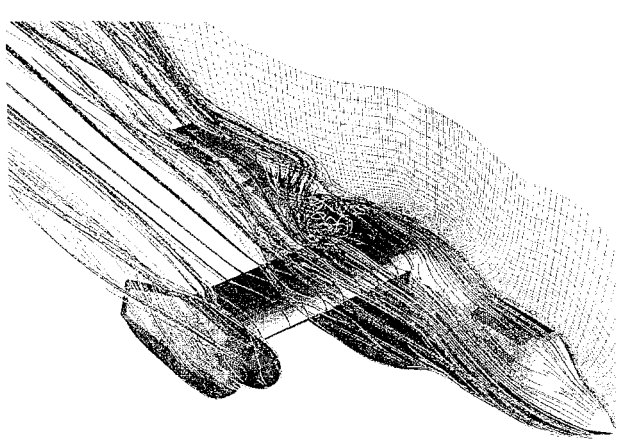

Fig. 7 Particle trace over the wing–fuselage–nacelle configuration at $\alpha = 12$ deg; perspective view.

For this particular case, i.e., at an angle of attack of 16 deg, a rear view of the particle trace of the flow is depicted in Fig. 9. This view, along with Fig. 8, gives a rather clear picture of the whereabouts of the free vortices resulting from flow separations over the wing, the fuselage, and the sponson. These vortices tend to merge into a single main vortex passing by the rear fuselage and the tail section. (The tail section is not shown and not included in the analysis.) The swirling of the flow after the wing–fuselage juncture has increased significantly by the crossflow, and therefore, a vortex breakdown may occur before the flow proceeds to the wake downstream. Vortex breakdown may occur during transient high-angle-of-attack maneuvers, even when no breakdown is observed in steady freestream at the same angle of attack.[20] Previous flight tests indicated the V-22 aircraft suffers a tail buffet problem during flight at high angles of attack. The vortex-breakdown-induced tail buffet, an unsteady phenomenon, is not considered in the present work. The results of particle trace presented provide first approximations to the position of the wing vortex with respect to the tail surface location, a clue to the cause of the tail buffet problem without considering the interaction of the wing vortices with the tail surfaces.

Velocity Vector

Velocity vector plots over the wing–fuselage–nacelle configuration at aforementioned angle-of-attack ranges are presented. At an angle of attack of 7 deg, the flow is attached as indicated in Fig. 10, where all of the velocity vectors at the wing root point in the streamwise direction with no flow reversal. The attached flow is sustained to an angle of attack of 12 deg from which a similar flow pattern is found. The wing

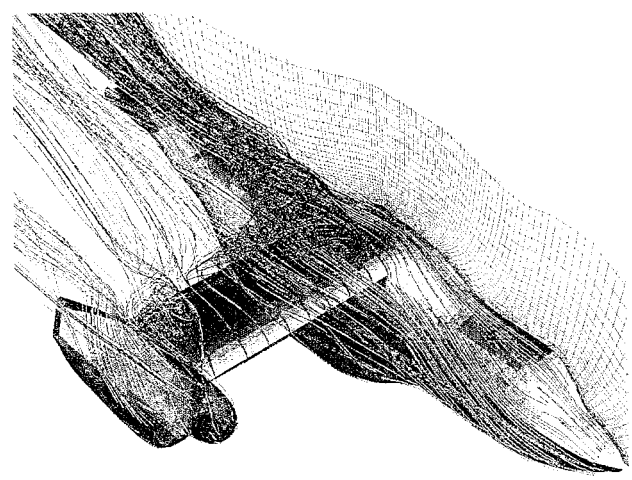

Fig. 8 Particle trace over the wing–fuselage–nacelle configuration at $\alpha = 16$ deg; perspective view.

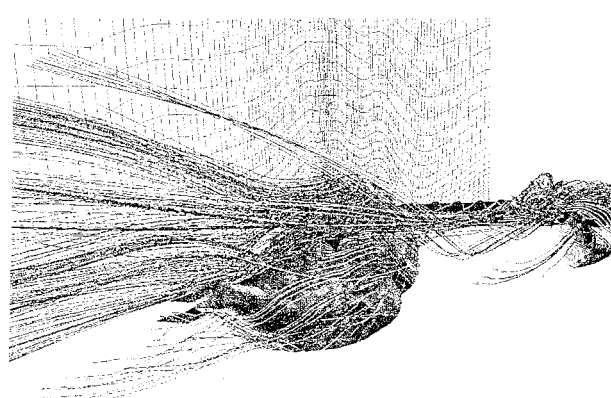

Fig. 9 Particle trace over the wing–fuselage–nacelle configuration at $\alpha = 16$ deg; rear view.

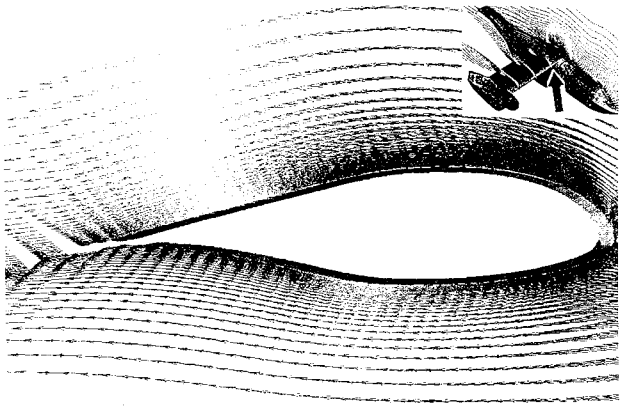

Fig. 10 Velocity vectors over wing root of the wing–fuselage–nacelle configuration at $M_\infty = 0.345$, $\alpha = 7$ deg, and $Re_\infty = 18.2 \times 10^6$.

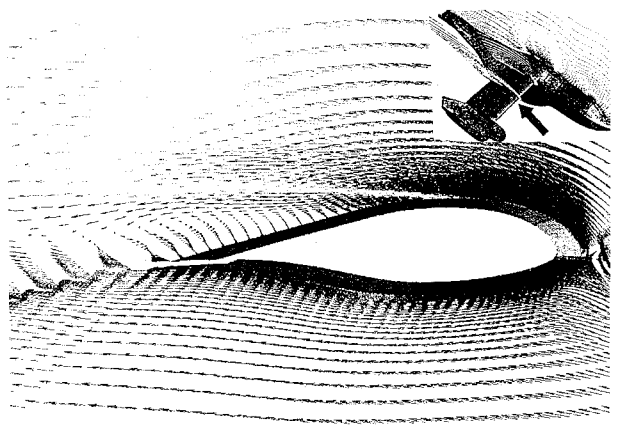

Fig. 11 Velocity vectors over wing midspan of the wing–fuselage–nacelle configuration at $\alpha = 16$ deg.

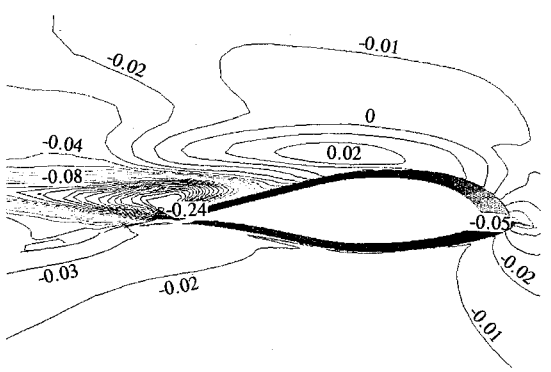

Fig. 12 Crossflow velocities over wing midspan of the wing–fuselage–nacelle configuration at $\alpha = 16$ deg.

section in Fig. 10 and similar plots are thickened to show airfoil contours.

This situation changes in the case of the 16-deg angle of attack. Velocity profiles and the corresponding crossflow components are examined with the aid of Figs. 11–14. The locations of these plots are at the wing midspan and the wing root. At the wing midspan, the flow approaches a zero velocity at the surface about a two-thirds chord length from the leading edge, and starts to reverse thereafter. The streamwise velocities form a vortex right above the trailing edge (see Fig. 11). The separation resembles that of the familiar two-dimensional boundary layer, but it belongs to the three-dimensional type because of the presence of crossflow components. The crossflow changes its direction from outboard in the fore region of the wing to inboard in the rear. Because of massive separation (vortex-layer-type separation as explained later), the crossflow velocities, which are normalized by the speed of sound, have increased sharply aft of the trailing edge (see Fig. 12).

Generally, the flow separation over the wing contains two types of separation: 1) the bubble type and 2) the vortex-layer type. The bubble-type separation is because of vanishing skin friction, whereas the vortex-layer type is caused by convergence of streamlines in the spanwise (crossflow) direction. Between the two, the vortex-layer-type separation usually prevails on the wing surface.[21,22] One symptom for the prevalence is that the line of crossflow reversal precedes the line of zero-skin-friction. This is the case here if we closely examine the velocities shown in Figs. 11–14, which give resultant velocity vectors and crossflow velocity contours at the wing midspan and wing root. The location of the zero-skin-friction moves from a two-thirds chord at the wing midspan to midchord at the wing root (see Figs. 11 and 13). The change of crossflow direction takes place from a two-thirds chord at the wing midspan to a one-third chord at the wing root (see Figs. 12 and 14). The flow is therefore dominated by the crossflow effect more than by the viscous effect. As a result, free vortices are created and proceed downstream, leaning toward the inboard spanwise direction. In the presence of the plane of symmetry of the aircraft, the crossflow would have to turn into the streamwise direction after passing the wing root, flourishing the swirling rate of the flow behind the wing–fuselage juncture.

Figure 15 shows the velocity vectors over the fuselage near the plane of symmetry of the aircraft. Here, there are no crossflow velocity components, and no vortex-layer type separation. The hump, as well as the front cockpit, speeds up the flow significantly. It eventually recovers smoothly without large flow reversals. The free vortices above the rear fuselage de-

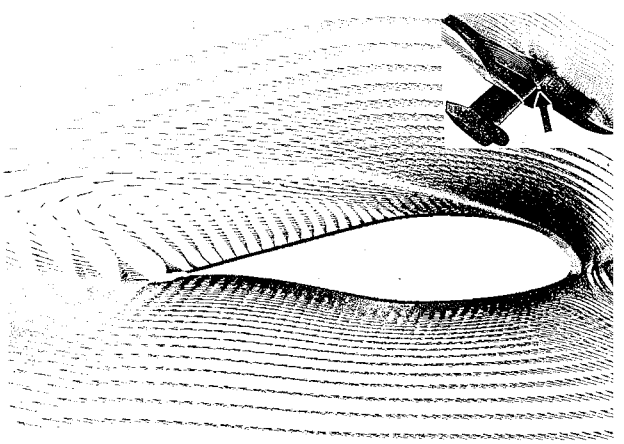

Fig. 13 Velocity vectors over wing root of the wing–fuselage–nacelle configuration at $\alpha = 16$ deg.

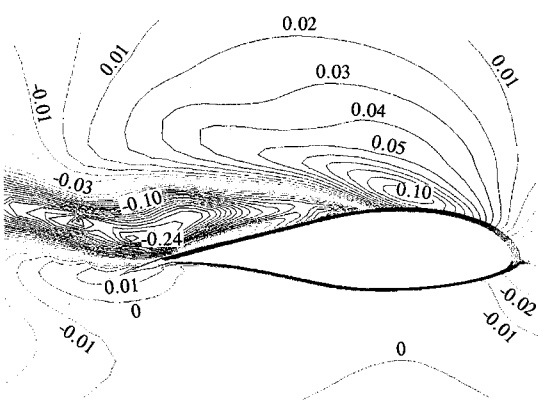

Fig. 14 Crossflow velocities over wing root of the wing–fuselage–nacelle configuration at $\alpha = 16$ deg.

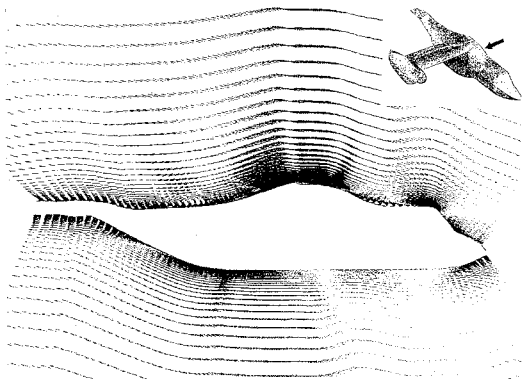

Fig. 15 Velocity vectors over the centerline of the wing–fuselage–nacelle configuration at α = 16 deg.

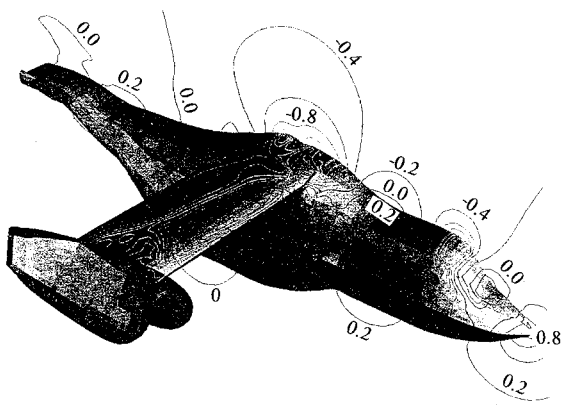

Fig. 16 Pressure distribution over wing–fuselage–nacelle configuration at M_∞ = 0.345, α = 16 deg, and Re_∞ = 18.2 × 10^6.

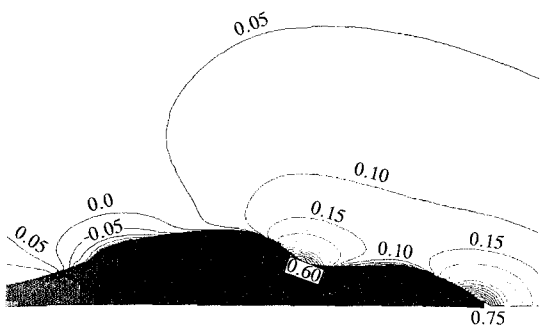

Fig. 17 Pressure distribution along sponson contour of the wing–fuselage–nacelle configuration.

picted by the particle trace result from other areas, rather than locally generated by the fuselage.

Pressure Distribution

The surface pressure distribution over the wing–fuselage–nacelle configuration for the case of an angle of attack of 16 deg is shown in Fig. 16. On the wing surface, peaky pressures appear in the leading-edge region, and a large positive pressure pocket in the inner part of the wing results from massive separation. In three-dimensional flows, the surface pressure influences the boundary-layer behavior in two ways: 1) the boundary layer being acted upon by the pressure distribution, i.e., the usual boundary-layer development; and 2) the viscous streamlines inside the boundary layer being acted upon by the external streamline pattern, which is dictated by the pressure gradients. The latter is intrinsic to three-dimensional flows and becomes more dominant when the vehicle is at a high angle of attack. The pressure pattern on the wing surface confirms the dominating vortex-layer-type separation in the inner rear portion of the wing.

The figure also displays the pressure coefficients over the symmetry plane along the fuselage. The high-pressure areas, indicated by positive values, are located in the nose–cockpit region and the fore fuselage hump. Since these areas have a front-facing projected area, positive pressures lead to a high aerodynamic drag. The hump region above the over-wing fairing has negative pressures, which can contribute to the overall lift of the aircraft. A smooth pressure recovery after the hump is consistent with the velocity vectors indicated in the previous figure, although the boundary-layer thickening is noticeable, but with no flow reversal.

Of particular interest is the pressure distribution along the sponson, this is shown in Fig. 17. Two positive pressure areas are observed: 1) one at the leading edge of the sponson and 2) the other at the shoulder. Like the fuselage contour, these front facing regions produce high-drag values. The low-pressure pocket after the midsponson also contributes to a drag increase.

Cross-sectional pressure distributions at three longitudinal locations, truncated at the zonal boundary for the nacelle, are selected to confirm the indications by the particle trace and velocity vector plots. Upstream of the sponson, which is also ahead of the wing, the pressure variation is smooth; pressure coefficients take on positive values in the lower region and start to decrease gradually above the interface plane (see Fig. 18). A high-pressure coefficient of 0.44, apparently caused by the presence of the sponson, is spotted at the lower left corner of the fuselage. In the forewing section, which is located just before the shoulder of sponson, the positive and negative pressure coefficients are clearly partitioned by the wing, as indicated in Fig. 19. The most negative pressures lie on the surface

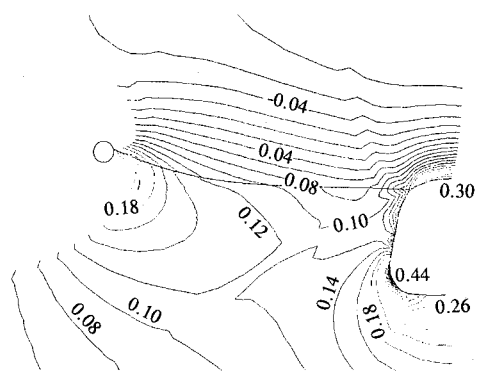

Fig. 18 Pressure distribution at fore-sponson section of the wing–fuselage–nacelle configuration.

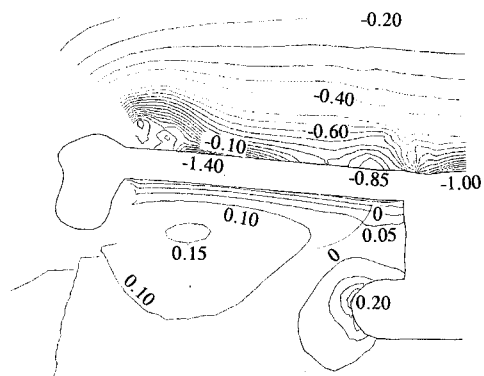

Fig. 19 Pressure distribution at fore-wing section of the wing–fuselage–nacelle configuration.

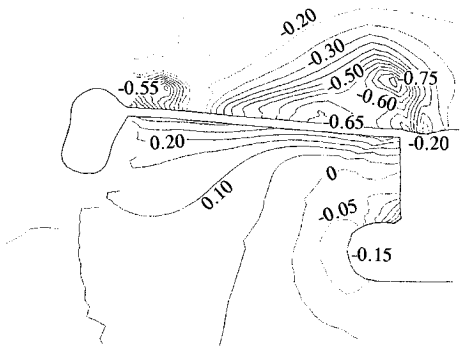

Fig. 20 Pressure distribution at rear-wing section of the wing–fuselage–nacelle configuration.

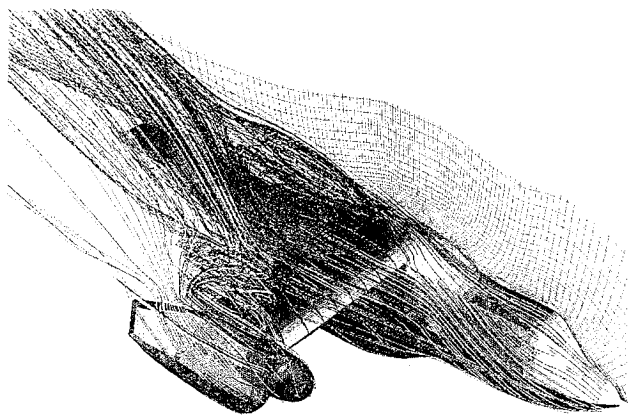

Fig. 21 Particle trace over the wing–fuselage–nacelle configuration at $M_\infty = 0.345$, $\alpha = 16$ deg, and $Re_\infty = 18.2 \times 10^6$ based on Spalart–Allmaras turbulence model.

indicating the flow thus far is attached. However, some crossflow activities start to take place near the wing–nacelle juncture and wing root. As we proceed downstream, the crossflow activity magnifies and massive flow separation becomes apparent as the low-pressure pockets develop above the wing surface (see Fig. 20).

Comparison of Turbulence Models

Results discussed were based on the Baldwin–Lomax turbulence model with the Degani–Schiff-type modification. As mentioned earlier, however, some convergence problems were encountered in cases of angles of attack of 12 and 16 deg. While these results are considered to be qualitatively correct, the case of the 16-deg angle of attack was also solved by using the Spalart–Allmaras one-equation turbulence model. The particle trace of the converged solution based on this model is shown in Fig. 21. Compared with that of Fig. 8, the S–A model yields more extensive viscous–inviscid interactions near the nacelle–wing juncture, but smaller crossflow velocities in the rear of the wing. The latter seems to contradict to flight-test measurements.

Concluding Remarks

The forward-flight flowfield of the V-22 tiltrotor aircraft is simulated by using a modern CFD technique. It is believed that the multizone, thin-layer Navier–Stokes method may serve as a practical tool for predicting the aircraft's aerodynamic performance with reasonable computer costs. Based on results obtained, which have been assessed with flight-test data qualitatively, some concluding remarks may be drawn:

1) The airfoil of the wing sections sustains attached flow at small-to-moderate angles of attack, which is good performance for such a very thick wing.

2) At high angle of attack, the vortex-layer-type separation resulting from the upper wing surface, the sponson, and the fore fuselage are strong to create free vortices that pass by the rear fuselage region, including the tail section. Vortex breakdown might occur causing breakdown-induced tail buffet.

3) High pressures are found in the front nose and midwing fairing (humped area) of the fuselage, as well as the leading edge and shoulder of the sponson. These pressures, along with flow separation over the wing, may result in high aerodynamic drag of the aircraft.

Further effort should include addition of the tail sections to the configuration, removal of the symmetric assumption for evaluating the sideslip effect, and extension to time-accurate computations to study the unsteady nature of vortex breakdown and its induced tail buffeting.

Acknowledgments

The present work was supported by the U.S. Naval Air Systems Command (Airtask A511-5115/010D/3H14250000) under the cognizance of S. A. Woods. The NASA NAS facility at Ames Research Center provided the Cray C-90 CPU time. The author wishes to thank M. A. McVeigh of Boeing Defense and Space Group, T. Wood of Bell Helicopter Textron, Inc., T. L. Holst of NASA Ames, and C. Rumsey of NASA Langley for useful discussions during the course of the present work.

References

[1]McVeigh, M. A., Grader, W. K., and Paisley, D. J., "Rotor Airframe Interactions on Tiltrotor Aircraft," *Journal of the American Helicopter Society*, Vol. 35, No. 3, 1990, pp. 43–51.

[2]Blohm, R., and Bartie, K., "V-22 Aerodynamic Report," Bell-Boeing Tiltrotor Team, Rept. 901-909-632, July 1986.

[3]Felker, F. F., Shinoda, P. R., Hefferman, R. M., and Sheehy, H. F., "Wing Force and Surface Pressure Data from a Hover Test of a 0.658-Scale V-22 Rotor and Wing," NASA TM 10244, Feb. 1990.

[4]Meyerhoff, C., and Gordge, D., "Navy Development Test (DT-IIA) of the MV-22 Aircraft, Contributory Test Report, Rotor Downwash," Naval Air Test Center, Tech. Rept. RW-71R-90, Patuxent River, MD, 1990.

[5]Grauer, W. K., and Farrell, M. K., "V-22 Flight Test Aerodynamics," *Proceedings of the 47th Annual Forum of the American Helicopter Society*, Vol. 1, American Helicopter Society, Washington, DC, 1991, pp. 101–106.

[6]Schleicher, D. R., and Alexander, H. R., "Technology Development for Advanced Tiltrotor Transports," AIAA Paper 93-4810, Dec. 1993.

[7]Raghavan, V., McCroskey, W. J., Van Dalsem, W. R., and Baeder, J. D., "Calculations of the Flow past Bluff Bodies, Including Tilt-Rotor Wing Sections at $a = -90$ Deg," AIAA Paper 90-0032, Jan. 1990.

[8]Fejtek, I., and Roberts, L., "Navier–Stokes Computation of Wing/Rotor Interaction for a Tilt Rotor in Hover," AIAA Paper 91-0707, Jan. 1991.

[9]Tai, T. C., and Vorwald, J., "Simulation of V-22 Rotorcraft Hover Flowfield," AIAA Paper 93-4878, Dec. 1993.

[10]Meakin, R., "Moving Body Overset Grid Methods for Complete Aircraft Tiltrotor Simulations," AIAA Paper 93-3350, July 1993.

[11]Sorenson, R. L., "The 3DGRAPE Book: Theory, Users' Manual, Examples," NASA TM 102224, July 1989.

[12]Flores, J., and Holst, T. L., "Numerical Solution of the Navier-Stokes Equations for Complex Configurations," *Lecture Series in Computational Fluid Dynamics*, Univ. of Tennessee Space Inst., Tulahoma, TN, March 1988.

[13]Thomas, J. L., Krist, S. T., and Anderson, W. K., "Navier-Stokes Computations of Vortical Flows over Low-Aspect-Ratio Wings," *AIAA Journal*, Vol. 28, No. 2, 1990, pp. 205–212.

[14]Baldwin, B., and Lomax, H., "Thin Layer Approximation and Algebraic Model for Separated Turbulent Flow," AIAA Paper 78-0257, Jan. 1978.

[15]Spalart, P., and Allmaras, S., "A One-Equation Turbulence Model for Aerodynamic Flows," AIAA Paper 92-0439, Jan. 1992.

[16]Rumsey, C. L., and Vatsa, V. N., "A Comparison of the Predictive Capabilities of Several Turbulence Models Using Upwind and Central-Difference Computer Codes," AIAA Paper 93-0192, Jan. 1993.

[17]Degani, D., and Schiff, L. B., "Computation of Supersonic Viscous Flows Around Pointed Bodies at Large Incidence," AIAA Paper 83-0034, Jan. 1983.

[18]Tai, T. C., "Theoretical Calculation of Viscous-Inviscid Transonic Flows," *Lecture Series on Shock-Boundary Layer Interaction in Turbomachines*, von Kármán Inst. for Fluid Dynamics, Brussels, Belgium, June 1980.

[19]Jenks, M. D., and Narramore, J. C., "Final Report for the 2-D Test of Model 901 Rotor and Wing Airfoils (BSWT 592)," Bell-Boeing Tiltrotor Team, Rept. D901-99065-1, July 1984.

[20]Visbal, M. R., "Onset of Vortex Breakdown Above a Pitching Delta Wing," *AIAA Journal*, Vol. 32, No. 8, 1994, pp. 1568–1575.

[21]Tai, T. C., and Walker, M., "On Three-Dimensional Flow Separation Criteria," AIAA Paper 91-1740, June 1991.

[22]Delery, J. M., "Physics of Vortical Flows," *Journal of Aircraft*, Vol. 29, No. 5, 1992, pp. 856–876.